ELSEVIER

Volume 180, Number 1, January 2007

JOURNAL OF SOLID STATE CHEMISTRY

www.elsevier.com/locate/jssc

CONTENTS

Abstracted/indexed in BioEngineering Abstracts, Chemical Abstracts, Coal Abstracts, Current Contents/Physics, Chemical, & Earth Sciences, Engineering Index, Research Alert, SCISEARCH, Science Abstracts, and Science Citation Index. Also covered in the abstract and citation database SCOPUS®. Full text available on ScienceDirect®.

Editorial Announcement

Regular Articles

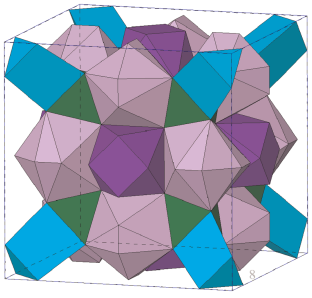

Representation of the $Li_{1.746}Nd_{4.494}FeO_{9.493}$ structure.

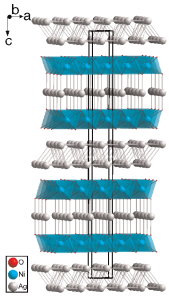

$Ag_3Ni_2O_4$—the first stage-2 intercalation compound of a delafossite.

Regular Articles—Continued

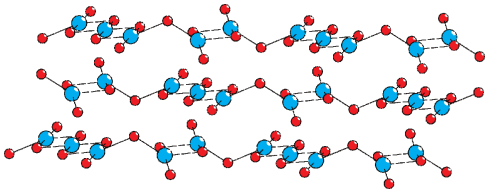

A novel copper silicate was synthesized through hydrothermal methods. Its crystal structure was determined from powder diffraction data. It comprises zig-zag chains of copper dimers and trimers. Its magnetic behavior is characteristic of one dimensional ferrimagentism. A magnetic exchange sequence is proposed based on structural arguments.

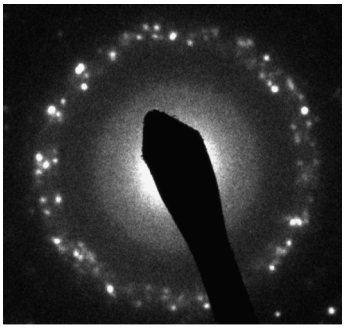

The decomposition of alumina-supported nickel glycinate in flowing argon mostly leads to an unusual phase of metallic Ni, hexagonal close-packed nanoparticles protected by graphite.

The synthesis and structural characterization of the new ternary nitrides: Ca_4TiN_4 and Ca_5NbN_5
Janet L. Hunting, Marta M. Szymanski, Philip E. Johnson, C. Brenhin Kellar and Francis J. DiSalvo
Page 31

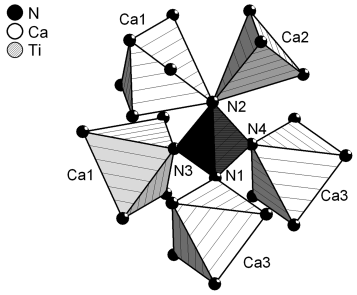

Ca_4TiN_4: titanium tetrahedron (center) corner-sharing with calcium polyhedra.

Structure and dielectric characterization of a new *A*-site deficient $La_{5/3}MgTaO_6$ perovskite
D.D. Khalyavin, A.M.R. Senos, P.Q. Mantas, D.N. Argyriou, I. Tarroso Gomes, L.G. Vieira and J.L. Ribeiro
Page 41

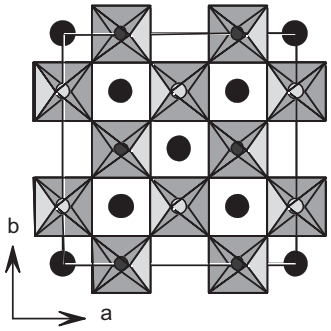

Short-range vacancy ordering and octahedral tilting in $La_{5/3}MgTaO_6$.

Ionothermal synthesis of β-NH_4AlF_4 and the determination by single crystal X-ray diffraction of its room temperature and low temperature phases
Emily R. Parnham, Alex M.Z. Slawin and Russell E. Morris
Page 49

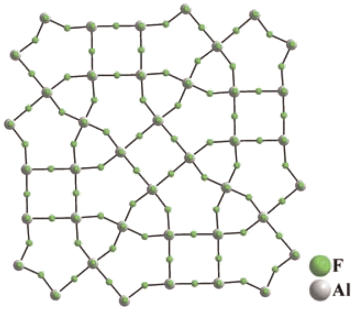

Ionothermal synthesis, the use of an ionic liquid as the solvent in materials preparation, has been used to prepare β-NH_4AlF_4, and structural characterisation indicates that there are two versions of the structure, a low temperature primitive phase at 93 K and a high temperature body-centered phase at 298 K.

Local structure and oxidation state of uranium in some ternary oxides: X-ray absorption analysis
A.V. Soldatov, D. Lamoen, M.J. Konstantinović, S. Van den Berghe, A.C. Scheinost and M. Verwerft
Page 54

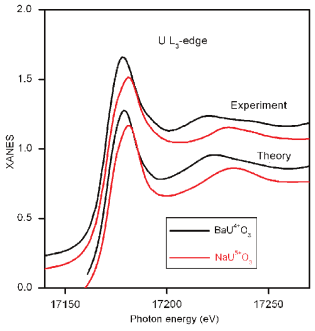

Comparison of the experimental U L_3 edge XANES in $BaUO_3$ and $NaUO_3$ with the theoretical spectra.

Syntheses, crystal and electronic structure, and some optical and transport properties of *Ln*CuOTe (*Ln* = La, Ce, Nd)
Min Ling Liu, Li Bin Wu, Fu Qiang Huang, Li Dong Chen and James A. Ibers
Page 62

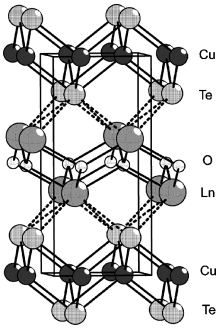

Crystal structure of *Ln*CuOTe viewed approximately along [1 0 0].

Product evolution in the Np(IV) fluorophosphate system
Travis H. Bray, Tyler A. Sullens, Tatiana Y. Shvareva, Richard E. Sykora, Richard G. Haire and Thomas E. Albrecht-Schmitt
Page 70

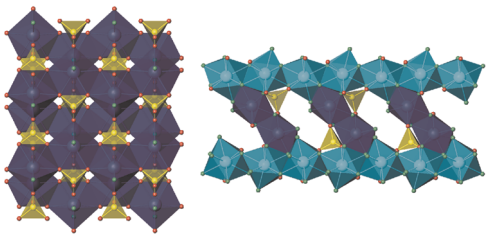

Two Np(IV) fluorophosphates, $NpFPO_4$ and $Cs_2Np_2F_7PO_4$, have been prepared as single crystals under hydrothermal conditions. $NpFPO_4$ crystallizes first, then reacts to yield $Cs_2Np_2F_7PO_4$ and finally yields NpF_4. Single crystal X-ray structures of $NpFPO_4$ and $Cs_2Np_2F_7PO_4$ show three-dimensional frameworks containing Np(IV) in both eight- and nine-coordinate environments.

Continued

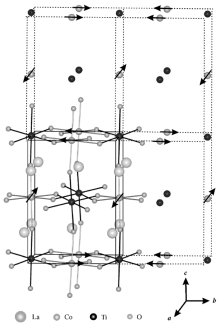

The antiferromagnetic structure of La_2CoTiO_6 as prepared by high-temperature routes with spins showing the $P2/m$' magnetic symmetry.

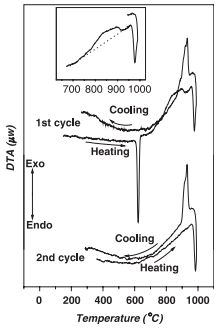

The cristobalite-type $GaPO_4$ relaxed slowly to quartz type modification above 700 °C (as indicated by a broad exotherm in inset).

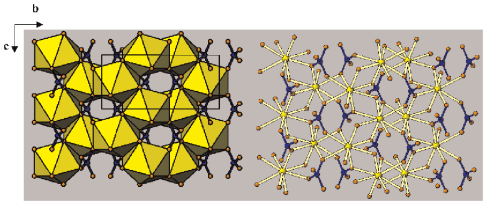

The scheelite-type structure of the new $NdWO_{3.05}N_{0.95}$ oxynitride prepared by the nitridation of corresponding $Nd_2W_2O_9$ precursor. The magnetic susceptibility for this oxynitride has been successfully simulated using the semi-empirical structure derived CF parameters.

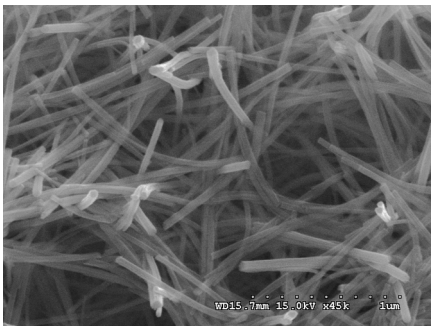

The large-scale synthesis of single-crystal hexagonal tungsten oxides nanowires has been successfully realized by a simple hydrothermal method without any templates and catalysts. Uniform h-WO_3 nanowires with diameters of 25–50 nm and length of up to several micrometers are obtained. The electrochemical performances of the nanowires as anode materials of Li-ion batteries have also been investigated. These 1D nanostructures exhibit better cycle ability than that of bulk materials, which indicates the morphology and particle size have the influences on the electrochemical performances.

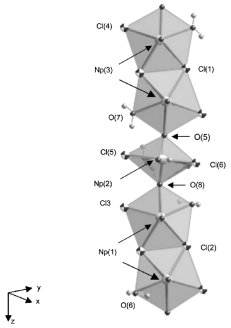

The structure of $K_4(NpO_2)_3Cl_7(H_2O)_4$ contains neptunyl pentagonal bipyramids that are linked into chains through cation–cation interactions.

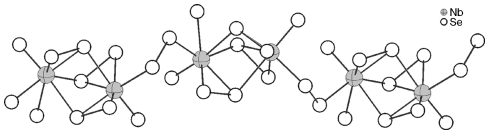

The $^1_\infty[Nb_2Se_{11}]^{4-}$ chain in the new mixed group1/group2 polyselenide compound $Rb_2BaNb_2Se_{11}$ is formed by interconnection of $[Nb_2Se_{11}]$ units via Se_2^{2-} dianions. The $[Nb_2Se_{11}]$ building blocks are formed by face sharing of two distorted pentagonal bipyramidal $NbSe_7$ groups.

Hydrothermal synthesis of lindgrenite with a hollow and prickly sphere-like architecture

Jiasheng Xu and Dongfeng Xue

Page 119

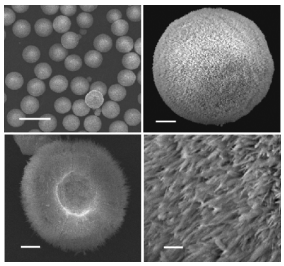

Lindgrenite $[Cu_3(OH)_2(MoO_4)_2]$ with a hollow and prickly sphere-like architecture has been synthesized via a hydrothermal route. The hierarchical lindgrenite particles are hollow and prickly spheres, which are comprised of numerous crystal strips that are aligned perpendicularly to the spherical surface. $Cu_3Mo_2O_9$ with the similar size and morphology can be easily obtained by a thermal treatment of the as-prepared lindgrenite.

Green and red upconversion luminescence in CeO_2:Er^{3+} powders produced by 785 nm laser

Hai Guo

Page 127

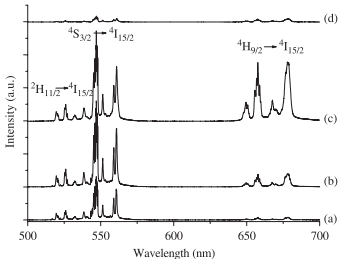

Upconversion spectra of Er^{3+}-doped CeO_2 powders with different Er^{3+} concentration: (a) 0.5% (b) 1% (c) 3% (d) 6%, (λ_{ex} = 785 nm).

Metal-organic frameworks from chiral square-pyramidal copper(II) complexes: Enantiospecific inclusion and perfectly polar alignment of guest and host molecules

Vamsee Krishna Muppidi, Panthapally S. Zacharias and Samudranil Pal

Page 132

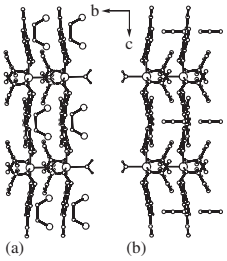

The square-pyramidal Cu(II) complexes $[CuL^n_2(H_2O)]$ with the bidentate HL^n (HL^1 = *N*-(2-hydroxy-5-nitrobenzyl)-(*R*)-α-methylbenzylamine and HL^2 = *N*-(2-hydroxy-5-nitrobenzyl)-(*S*)-α-methylbenzylamine) form 1:1 host–guest compounds with $Br(CH_2)_2Br$ and CH_3CN. The X-ray structures of these species reveal the enantiospecific confinement of the chiral rotamers of $Br(CH_2)_2Br$ and perfectly polar ordering of both host and guest molecules in the crystal lattice. The figure shows the polar alignments of (a) $[CuL^1_2(H_2O)] \cdot (P)\text{-}C_2H_4Br_2$ and (b) $[CuL^2_2(H_2O)] \cdot CH_3CN$.

$EuBaFe_2O_5$: Extent of charge ordering by Mössbauer spectroscopy and high-intensity high-resolution powder diffraction

P. Karen, K. Gustafsson and J. Lindén

Page 138

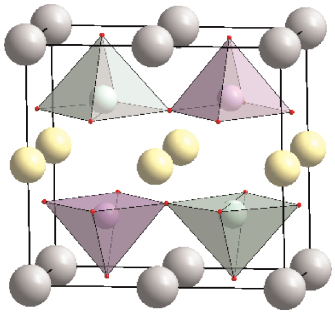

Environments of the two crystallographically different Fe atoms in charge-ordered $EuBaFe_2O_5$ at 100 K as refined from SXPD data; distances in Å.

$EuBaFe_2O_{5+w}$: Valence mixing and charge ordering are two separate cooperative phenomena

P. Karen, K. Gustafsson and J. Lindén

Page 148

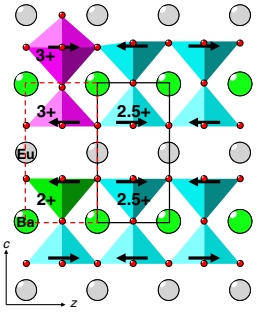

Effect of oxygen nonstoichiometry on valence mixing of di- and trivalent iron via electron sharing in ferromagnetically coupled pairs across the Eu layer in $EuBaFe_2O_{5+w}$.

Chemical twinning of the pyrochlore structure in the system Bi_2O_3–Fe_2O_3–Nb_2O_5

I.E. Grey, W.G. Mumme, T.A. Vanderah, R.S. Roth and C. Bougerol

Page 158

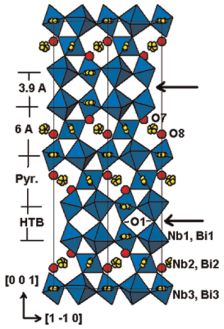

Polyhedral representation of the hexagonal $Bi_{5.67}Nb_{10}FeO_{35}$ structure, viewed along [1 1 0]. Arrows show location of chemical twin planes. Bi atoms are shown as clusters of small circles. O′ atoms (O(7), O(8)) are shown as larger circles.

Continued

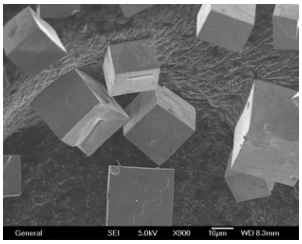

The calcium-doped manganates, $Pr_{1-x}Ca_xMnO_3$ ($x = 0.39$, 0.46, 0.70, 0.76), were synthesized as cube-shaped crystalline phases under mild hydrothermal conditions for the first time. The crystals could be grown in one step from solutions of metal salts and potassium hydroxide solution at temperatures ~240 °C. The studies indicate that formation of the materials is dependent on the alkalinity and composition of the initial reaction mixtures. The magnetic properties show spin-glass-like behavior due to competing ferromagnetic and antiferromagnetic exchange interactions in $Pr_{1-x}Ca_xMnO_3$ with $x = 0.39$, 0.46.

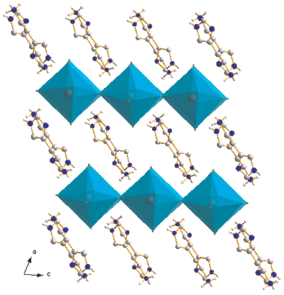

Structure and optical properties of new layered organic–inorganic haloplumbate complexes,which combine haloplumbate and organic ammonium of histaminium and 3-amino-1,2,4-triazol were systematically studied.

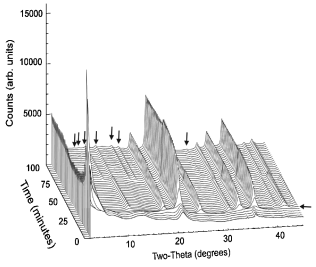

Stack of powder diagrams showing the formation of γ-Fe_2O_3 nanoparticles and subsequent vacancy ordering at 305 °C.

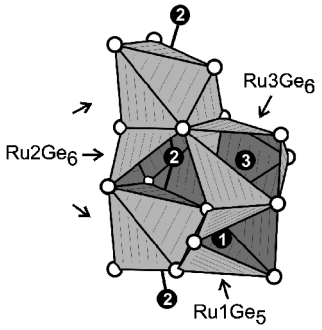

Condensation of the $Ru1Ge_5$, $Ru2Ge_6$, and $Ru3Ge_6$ units in the structure of $Yb_2Ru_3Ge_4$.

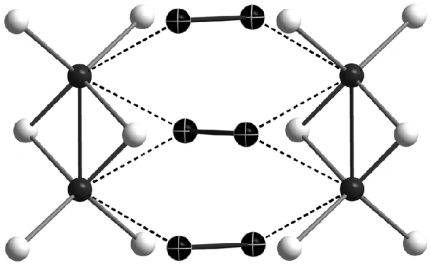

The metallic selenide Pd_2CoSe_2 and homologue Pd_2MCh_2 compounds (M = Fe, Co, Ni; Ch = Se, Te) are the first ternary palladium chalcogenides with iron group metals. The crystal structure shows one-dimensional $^1_\infty[CoSe_{4/2}]$ tetrahedra with short Co–Co bonds, which are connected by Pd_2 dumbbells. Electronic structure calculations reveal strong metal–metal bonding.

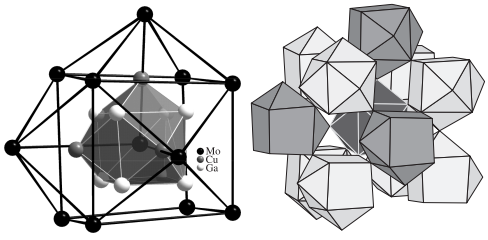

Threefold capped cubes $TMCu_3Ga_8$ are the coordination polyhedra in the new compounds $TM_2Cu_3Ga_8$ (TM = V, Mo, W) which were synthesised from the elements. The new crystal structure can be described as an ordered defect variant of the bcc packing: $[(TM)_2(Cu)_3(\square)_3][Ga_8]$. As a motif of self-similarity the polyhedra itself are packed in the same way.

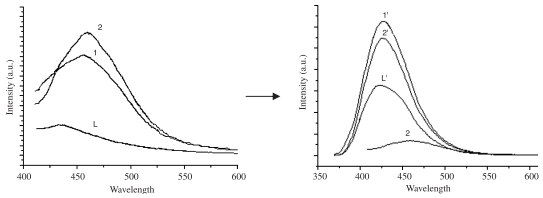

Two novel Pb(II) complexes: $\{[Pb(hca)_2 \cdot DMF] \cdot DMF\}_\infty$ and $[Pb(hca)_2(phen) \cdot DMF]_2$, (hca = trans-4-hydroxycinnamic anion) were obtained and characterized. Their structures are also determined by X-ray crystal analysis. Both of complexes in DMF solution show visible fluorescence and the intensity is stronger than that of ligand. Their emission intensities are increased greatly in an alkaline solution of pH 8, which is due to the enhancement of the planar conjugation of ligand hca with the deprotonate of the phenolic group.

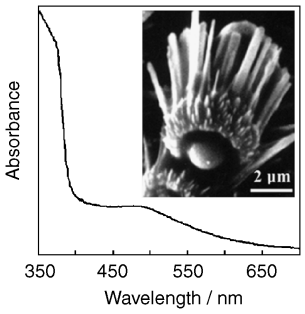

One-step solvothermal synthesis of novel comet-like superstructures of radially standing ZnO submicron rod arrays.

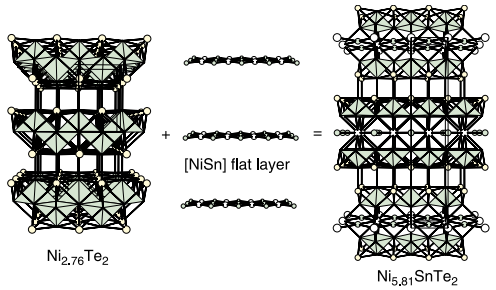

Modulated crystal structure of $Ni_{5.81}SnTe_2$ can be virtually generated from that of $Ni_{2.76}Te_2$.

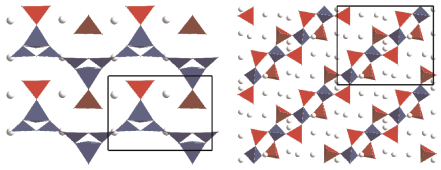

Two new anhydrous sodium borophosphates $Na_3B_6PO_{13}$ and $Na_3BP_2O_8$ were synthesized by low-temperature molten salts techniques using boric acid and sodium dihydrogen phosphate as flux, respectively. $Na_3B_6PO_{13}$ crystallize in *Pnma* and comprise infinite chain of $^1_\infty\{[B_6PO_{13}]\}^{3-}$, and $Na_3BP_2O_8$ crystallize in *C*2/*c* and comprise infinite chain of $^1_\infty\{[BP_2O_8]\}^{3-}$.

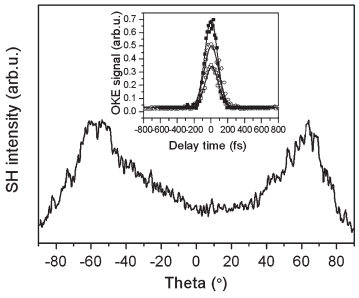

Second-harmonic generation (SHG) has been observed from thermally poled $Ge–Ga–S–PbI_2$ glasses by utilizing Maker fringe method. Ultrafast third-order nonlinear optical responses of these glasses have been measured by using femtosecond time-resolved optical Kerr effect (OKE) technique at the wavelength of 820 nm.

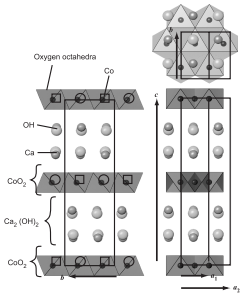

Crystal-structure model of the misfit-layered cobalt oxide $(CaOH)_{1.14}CoO_2$. The rectangles indicate unit cells of the two subsystems. The open circles and squares represent the cobalt atoms situated at different positions along the projected coordinate.

Continued

An organically templated yttrium fluoride with a 'Super-Diamond' structure
Nicholas F. Stephens and Philip Lightfoot
Page 260

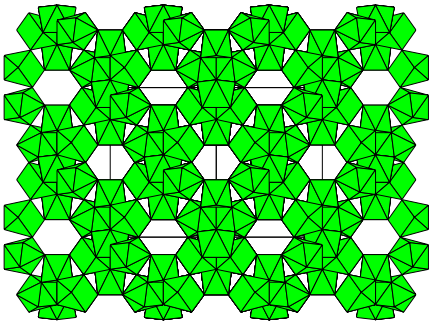

The organically templated yttrium fluoride $[C_3N_2H_{12}]_{0.5}[Y_3F_{10}]$ adopts a 'Super-Diamond' framework structure. Its hydrothermal synthesis and structure determination from powder X-ray diffraction (PXRD) are described.

Structural characterization, thermal and electric properties of imidazolium bromoantimonate(III): $[C3H_5N_2]_3[Sb_2Br_9]$
A. Piecha, V. Kinzhybalo, K. Ślepokura and R. Jakubas
Page 265

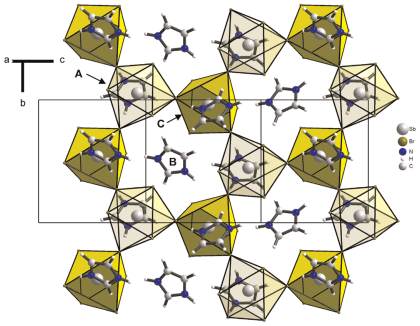

Projection of the crystal structure of $[C_3H_5N_2]_3[Sb_2Br_9]$ at 100 K (form I) on the cb plane as a polyhedral representation.

Nanosized aluminum nitride hollow spheres formed through a self-templating solid–gas interface reaction
Jie Zheng, Xubo Song, Yaohua Zhang, Yan Li, Xingguo Li and Yikang Pu
Page 276

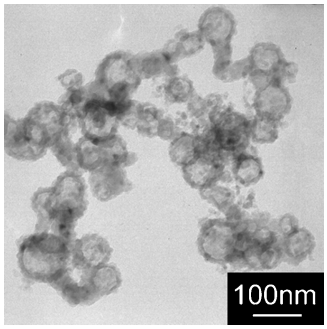

Nanosized aluminum nitride hollow spheres were synthesized by nitridation of aluminum nanoparticles at 1000 °C using ammonia.

Microemulsion-mediated hydrothermal synthesis and characterization of zircon-type $LaVO_4$ nanowires
Weiliu Fan, Xinyu Song, Sixiu Sun and Xian Zhao
Page 284

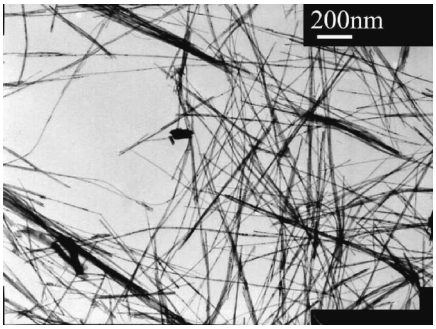

The zircon-type tetragonal (*t*-) $LaVO_4$ nanowires were controlled synthesized by a microemulsion-mediated hydrothermal method, in which the aqueous cores of SDS/cyclohexane/*n*-hexanol/water microemulsion were used as constrained microreactors for a controlled growth of *t*-$LaVO_4$ nanocrystals under hydrothermal conditions.

Nanoparticles of superconducting γ-Mo_2N and δ-MoN
A. Gomathi, A. Sundaresan and C.N.R. Rao
Page 291

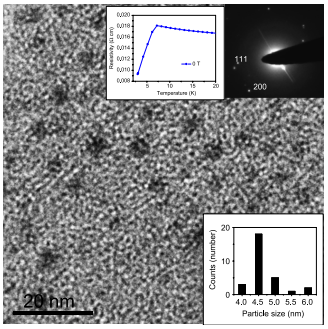

TEM image of the γ-Mo_2N particles with the inset showing the resistivity of the sample as a function of temperature.

Cation distribution and magnetic properties in chromium-substituted nickel ferrites prepared using aerosol route
Sonal Singhal and Kailash Chandra
Page 296

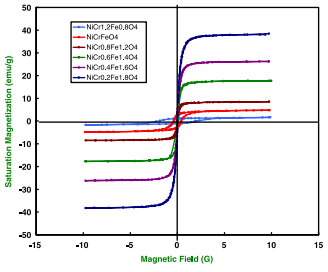

Hysterisis loop of chromium-substituted nickel ferrites after annealing at 1200 °C.

Fabrication and characterization of cerium-doped barium titanate inverse opal by sol–gel method
Yi Jin, Yihua Zhu, Xiaoling Yang, Chunzhong Li and Jinghong Zhou
Page 301

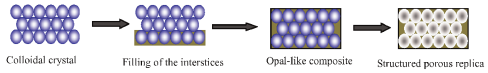

Cerium-doped barium titanate inverted opal was synthesized from barium acetate acid contained cerous acetate and tetrabutyl titanate in the interstitial spaces of a PS opal, which involves infiltration of precursors into the interstices of the PS opal template and removal of the PS opal by calcination.

Synthesis and structure determination of $Co(HNCN)_2$ and $Ni(HNCN)_2$
Manuel Krott, Xiaohui Liu, Paul Müller and Richard Dronskowski
Page 307

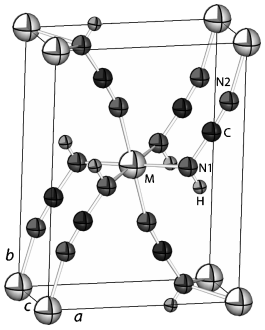

Crystal structure of $Co(HNCN)_2$ and $Ni(HNCN)_2$ with Co/Ni atoms as white, N as grey, C as dark-grey, and H as light-grey balls.

Structure and electron density analysis of electrochemically and chemically delithiated $LiCoO_2$ single crystals
Yasuhiko Takahashi, Norihito Kijima, Kaoru Dokko, Matsuhiko Nishizawa, Isamu Uchida and Junji Akimoto
Page 313

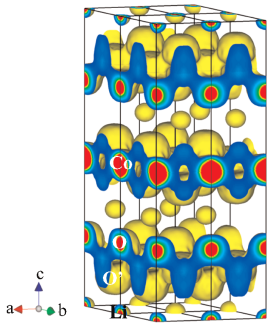

Three-dimensional electron density distribution of the electrochemically delithiated $Li_{0.68}CoO_2$ obtained by the maximum entropy method (MEM) using single-crystal X-ray diffraction data.

Structural characterization of the hollandite host lattice for the confinement of radioactive cesium: Quantification of the amorphous phase taking into account the incommensurate modulated character of the crystallized part
A.Y. Leinekugel-le-Cocq-Errien, P. Deniard, S. Jobic, E. Gautier, M. Evain, V. Aubin and F. Bart
Page 322

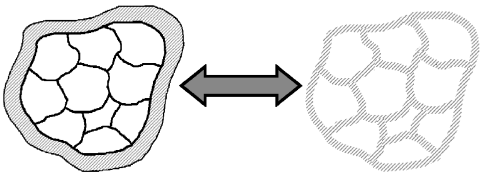

Amorphous phase localization.

Unusual one-dimensional branched-chain structures assembled by a novel imidazole-containing tripodal ligand with cadmium(II) salts and their fluorescent property
Ling-Yan Kong, Xi-Hong Lu, Yong-Qing Huang, Hiroyuki Kawaguchi, Qian Chu, Hui-Fang Zhu and Wei-Yin Sun
Page 331

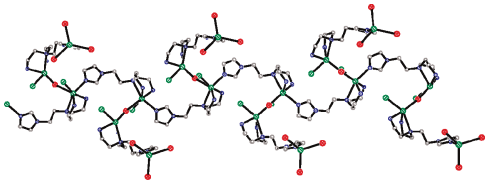

Three novel coordination polymers $[Cd_3(L)_2(\mu\text{-}Br)(\mu\text{-}Cl)Br_3Cl]$ (**1**), $[Cd_3(L)_2(\mu\text{-}Cl)_2Cl_4]$ (**2**) and $[Cd(L)Cl]_2[CdCl_4]\cdot H_2O$ (**3**) with one-dimensional branched chain and zigzag chain structures were obtained by reactions of an imidazole-containing tripodal ligand N^1-(2-aminoethyl)-N^1-(2-imidazolethyl)-ethane-1,2-diamine (L) with Cd(II) salts.

Mössbauer spectra as a "fingerprint" in tin–lithium compounds: Applications to Li-ion batteries
F. Robert, P.E. Lippens, J. Olivier-Fourcade, J.-C. Jumas, F. Gillot, M. Morcrette and J.-M. Tarascon
Page 339

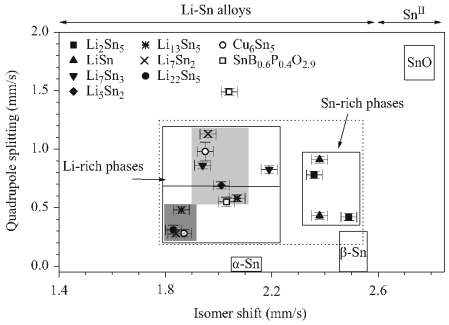

$\Delta-\delta$ correlation diagram for the different tin sites of the Li–Sn compounds. The symbols denote the different Li–Sn phases and the products obtained at the end of the discharge of η-Cu_6Sn_5 and $SnB_{0.6}P_{0.4}O_{2.9}$. The grey and the light-grey areas show Sn-centred polyhedra without and with one Sn first-nearest neighbours, respectively.

Continued

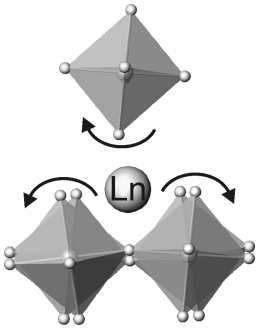

Tilting of the octahedra in K_2NiF_4 structure type oxides (A_2BO_4) may be controlled by the A-type cation size and by temperature.

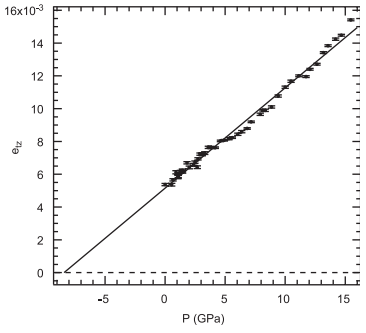

Variation of the tetragonal strain, e_{tz}, as a function of pressure for $Ca_{0.35}Sr_{0.65}TiO_3$, showing a break in slope in the vicinity of 3–4 GPa.

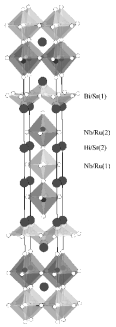

Structure of $Bi_{1.5}Sr_{2.5}Nb_{2.5}Ru_{0.5}O_{12}$.

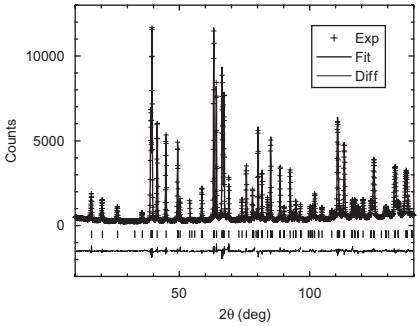

Powder neutron diffraction patterns of $Ag_5Pb_2O_6$ at room temperature.

Rapid Communication

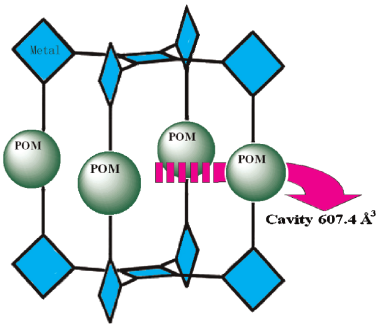

The boxlike structure of compound **1** with cavity is designed from $[\{Ni(en)_2\}_4(4,4'\text{-bipy})_4\{Ni(H_2O)_2\}]$ sheets pillared by $[\alpha\text{-}As_8V_{14}O_{42}]$ clusters, which represents the first mixed-organic ligand-decorated tetrameric As–V–O cluster.

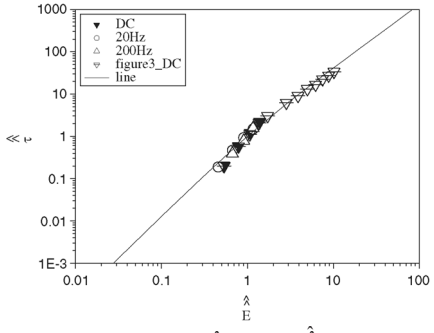

Universal yield stress plot of $\hat{\tau}$ versus $\hat{E}$ for triethanolamine-modified TiO_2 based on ER fluid various electric fields.

Synthesis, structure and photochromic properties of a novel 1,6-hexanediamine trimolybdate supramolecular compound
Dehui Sun, Hongjie Zhang, Jilin Zhang, Guoli Zheng, Jiangbo Yu and Shuyan Gao
Page 393

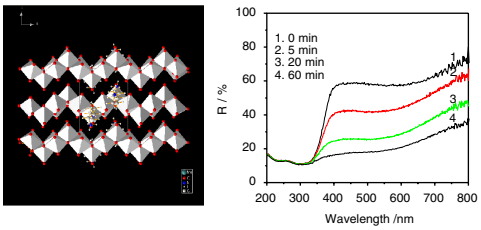

Crystal structure of 1,6-hexanediamine trimolybdate $(C_6H_{18}N_2)[Mo_3O_{10}]$ along *c*-axis. It consists of protonated 1,6-hexanediamine (HDA) and novel infinite chains $[Mo_3O_{10}]^{2-}$. Infinite chains $[Mo_3O_{10}]^{2-}$ are made up of distorted MoO_6 octahedron connected by edges and corners and are linked through protonated HDA cations into a one-dimensional network. What is more, the compound displays photochromic properties and may be applied to the field of photosensitive materials.